Cucurbit[8]uril as Supermolecular Lock for Design Dual-chain Conjugated Polymer as Enhanced H_2O_2 Production Photocatalyst.

Jie Yin, Sizhe Li, Hao Zhang, Yao Lu, Yan Zhao*, K. A. I. Zhang

Department of Materials Science, Fudan University 200433 Shanghai (P. R. China).

Synthesis of CB[8]:

In a typical experiment, cucurbit[8]uril (CB[8]) were synthesized and purified based on the described earlier by Kim et al.[1] Urea and glyoxal were dissolved in HCl (3 M in water) and heated at 80 °C in an oil bath for the synthesis of glycoluril. The glycoluril (300 g, 2.11 mol) was dissolved in conc. HCl (500 mL) and heated at 80 °C. And then was added dropwise with a PD solution (135, 4.49 mol in conc. HCl). The system was heated at 80~85 °C for 2 h and then at 105 °C for 24 h. After addition of acetone/water mix solution (1.0 L), CB homologues mixture was removed by filtration. The CB[8] was separated from the other CB homologues mixture through successive recrystallisations from HCl solution (3 M, 6 M in water) followed by a final recrystallisation from H_2O/acetone.

Synthesis of d-DTP-CB[8] (encapsulation complex of two DTP within CB[8]):

A mixture containing CB[8] (0.145 g, 0.1 mmol), DTP (0.057 g, 0.22 mmol), acetic acid (14 mL), and Milli-Q grade water (70 mL) was prepared and transferred to a Schlenk flask. The flask was then rapidly cooled using liquid nitrogen to a temperature of o77 K and evacuated to a pressure of 400 mTorr. Subsequently, the flask was purged with argon gas multiple times. The flask was then heated to 60 °C in an oil bath while continuously stirring for 2 h. As the reaction proceeded, the initially turbid suspension gradually clarified. After completion of the reaction, the solution was rapidly frozen with liquid nitrogen and transferred to a freeze dryer for 36 h for freeze-drying. The resulting product obtained was a white powder.

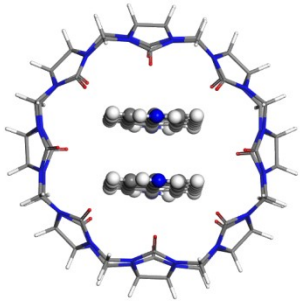

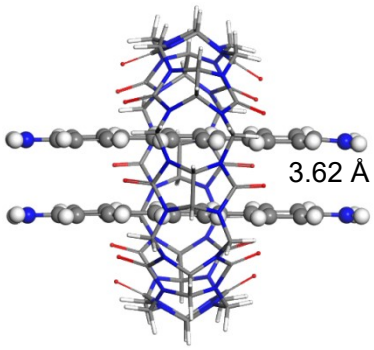

Calculation of photoluminescence lifetime:

The emission at the band-edge of four different types of CPs exhibits decay through both radiative and nonradiative electron-hole recombination processes. The decay behavior at 450 nm was analyzed using a biexponential model, represented by the equation:

$$I(t) = B_1 \exp\left(-\frac{t}{\tau_1}\right) + B_2 exp(-\frac{t}{\tau_2})$$

where I(t) represent the intensity, τ_1 and τ_2 are the decay times, and B_1 and B_2 represent the relative magnitudes. By studying the dynamics of exciton transfer, the decay curves of a material were analyzed using a biexponential kinetics function. This function revealed two decay components, with τ_1 and τ_2 corresponding to the nonradiative recombination of charge carriers and the recombination of free excitons, respectively.

Transient Absorption Spectroscopy:
The femtosecond transient absorption data were acquired using a HELIOS ultrafast pump-probe system. The pump pulse source utilized an amplified femtosecond laser system with a minimum step size of 2.2 fs and a maximum speed of 10 ns s^{-1}, operating at a rate of 5 kHz and a wavelength of 800 nm. The pump pulses were generated by an optical parametric amplifier (TOPAS-800-fs). The white light continuum probe beam was generated by focusing a small portion (~10 μJ) of the regenerative amplifier's fundamental 800 nm laser pulses into a 2 mm sapphire crystal. To ensure high signal-to-noise ratios, the data was collected by conducting measurements within a range of 5 to 10 scans. Furthermore, the signal amplitudes obtained from the fs-TA measurements were averaged for subsequent analysis. The CPs were dispersed in deoxygenated DMF at a concentration of approximately 0.05 mg mL^{-1} and subjected to sonication for 30 minutes to achieve well-dispersed solutions for measurements.

In Situ diffuse reflectance infrared Fourier transform spectroscopy Characterization:
In situ diffuse reflectance infrared Fourier transform spectroscopy (DRIFTS) measurements were conducted using the Bruker INVENIOR FT-IR spectrometer equipped with an in situ diffuse reflectance cell (Harrick). The specimens were placed within a specially designed infrared reaction chamber that was specifically created for the analysis of powder samples that exhibit significant scattering properties in the diffuse reflection mode. The reaction chamber was hermetically sealed using two ZnSe windows to facilitate the transmission of incident light. The chamber was filled with oxygen and water vapor prior to an in-situ reaction. A Xe lamp (λ>420 nm) was used as the light source.

Electron paramagnetic resonance (EPR) measurements:
Spin trapping-EPR tests were recorded using a Bruker EMX plus-6/1 model spectrometer operating at the X-band frequency (9.4 GHz). 5,5-dimethyl-1-pyrroline N-oxide (DMPO) was used as a spin-trapping reagent to detect •OH or $O_2^{\bullet-}$, while 4-oxo-2,2,6,6-tetramethylpiperidine (TEMP) was used to detect $^1O_2$. The catalysts were dispersed in the deionized water (DI) to prepare aqueous solution with a concentration of 1 mg mL^{-1}. The dispersion and spin-trapping reagent were mixed in equal volumes, and the resulting mixture was aspirated using a capillary tube and transferred into a quartz tube. Subsequently, the quartz tube was inserted into the sample chamber. A Xe lamp (λ>420 nm) was used as the light source. The dispersion was purged with Ar or O_2 gas for 20 min before light irradiation.

H_2O_2 production：
The 10 mg photocatalyst was dispersed in a 10 ml aqueous solution and transferred to a 25 mL Schlenk flask. The suspension was then well dispersed by ultrasonication for 10 min. After that, O_2 was bubbled into the suspension

for 20 min in the dark. The oxygen was connected to the Schlenk flask through a three-way valve with a balloon to provide continuous oxygen supply. Prior to the photocatalytic reaction, a dark reaction was conducted for 30 min to promote the equilibrium of the photocatalytic system. The suspension was irradiated by a blue LED lamp (420 nm, 340 mW cm^{-2} Kessil RoHS) during photoreaction. The concentration of H_2O_2 was determined using a UV-vis spectrophotometer. For example, sample was filtered through a 0.42 μm filter to remove the photocatalysts. 100 μL of the filtrate was then diluted to a final volume of 1.9 mL using phosphate-buffered saline (PBS, pH=7.4). To this diluted sample, 50 μL of N,N-diethyl-l,4-phenylenediammonium sulfate salt (DPD) solution and 50 μL of peroxidase from horseradish (POD) solution were added simultaneously. The resulting solution was transferred into 1 cm quartz cell to measure the absorbance (400–650 nm) using a UV-vis spectrophotometer.

Isotope labeling experiments for H_2O_2 production:

The catalyst (2 mg) and 1 mL of $H_2{}^{18}O$ (97%) were placed in a sealed apparatus consisting primarily of a quartz tube and sealing components. The suspension was bubbled with O_2 and ultrasonicated in the dark for 30 minutes to reach adsorption-desorption equilibrium. After 1 hour of irradiation with an LED light source, the catalyst was separated from the suspension. The formed hydrogen peroxide was catalytically decomposed to O_2 and H_2O using MnO_2 in a sealed container under an Ar atmosphere. The gas products in the headspace of the reaction vessel were analyzed by GC-MS.

Determination of H_2O_2 concentration:

DPD and POD reagents were freshly prepared and stored in the dark at ~4 °C as follow: 0.1 g of N,N-diethyl-l,4-phenylenediammonium sulfate salt (DPD) were dissolved in 10 mL of 0.05 M H_2SO_4, and 10 mg of peroxidase from horseradish (POD) were dissolved in 10 mL of distilled water.

The H_2O_2 concentration was determined using the following mechanism: DPD can be transformed by H_2O_2/POD into magenta $DPHD^{+\cdot}$ (as shown in Scheme 1). Therefore, the concentration of $DPHD^{+\cdot}$ after the photoreaction can be measured using a UV-vis spectrophotometer, with the maximum absorption peaks centered at around 510 nm and 551 nm.

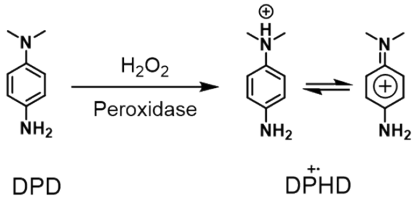

Scheme S1 Max abs. of DPD was at 260 nm, oxidized forms of DPD max abs. at 510 nm and 551 nm.

Generating the standard curve: A 1 mmol L^{-1} H_2O_2 aqueous solution was prepared. Aliquots of 20, 40, 60, 80, 100, and 120 μL were taken and diluted to 1.9 mL with PBS buffer. Then, 50 μL of DPD and 50 μL of POD were added to each solution. The resulting solutions were measured for absorbance in the range of 400-650 nm using a UV-vis spectrophotometer. Based on the absorbance at 510 nm and the actual concentration of H_2O_2, a standard curve for H_2O_2 concentration was plotted.

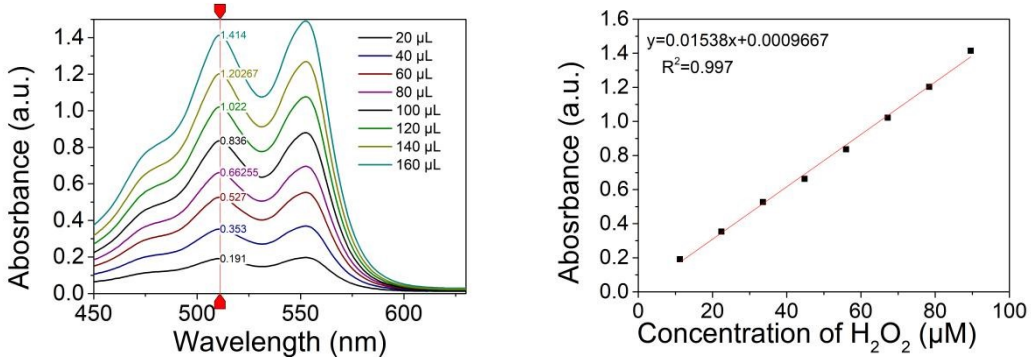

Schenme S2 Illustration of standard curves.

Photoelectrochemical and Electrochemical Measurements:

All the measurements performed using an Autolab PGSTAT204 potentiostat/galvanostat (Metrohm) in a three-electrode cell system. Standard three-electrode setup consists of a ITO electrode as the working electrode, a platinum mesh as the counter electrode and a Ag/AgCl (in saturated KCl solution) electrode as the reference electrode. Illumination source is a 300 W Xe lamp.

Rotating disk electrode (RDE) measurements:

Electrochemical characterization was executed on an electrochemical workstation (Autolab Metrohm, Germon) with a general three electrode system at room temperature. A glassy carbon rotating disk electrode with loading of catalyst (Autolab Metrohm, Germon) was utilized as the working electrode. While reference electrode and counter electrode were referred to Hg/Hg_2Cl_2 electrode and platinum mesh electrode, respectively.

The catalyst ink was prepared by mixing 10 mg catalyst, 225 μL isopropyl alcohol, 255 μL ultrapure water and 20 μL Nafion (5 wt%, Alfa) together, then ultrasonicated for 1 h. All linear sweep voltammetry (LSV) were acquired by testing with different rotating rate at 400-1600 rpm in the in an O_2-saturated 1 M KCl solution at room temperature, with a scan rate of 10 mV s^{-1} and varying rotation speeds after bubbling O_2 for 1 hour. During the reaction, a LED light source vertically illuminated the rotating electrode, enabling the acquisition of photoelectrochemical kinetic information and the observation of peroxide formation. RDE technique was conducted to measure the kinetic current density

(J_k) and electron transfer numbers (n) in the ORR process, which was calculated from the following Koutecky-Levich equation:

$$\frac{1}{J} = \frac{1}{J_L} + \frac{1}{J_{K=}} \quad \frac{1}{B\omega^{1/2}} + \frac{1}{J_K}$$

$$B = 0.62nFC_0{D_0}^{2/3}\upsilon^{-1/6}$$

where, J (A cm^{-2}) represents the measured current density, the J_K and J_L represent the kinetic and diffusion-limiting current densities. The symbols ω, F, C_0, D_0, and ν represent the angular velocity, Faraday constant (96485.3 C mol^{-1}), bulk concentration of O_2 (1.26×10^{-6} mol cm^{-3}), diffusion coefficient of O_2 in 1 M KCl solution (1.84×10^{-5} cm^2 s^{-1}),[2] and kinetic viscosity of the electrolyte (0.01 cm^2 s^{-1}), respectively.

Rotating ring-disk electrode (RRDE) measurements:

The working electrode of the Rotating Ring-Disk Electrode (RRDE) consists of a 5 mm glassy carbon disk, with a gap of 375 μm between the disk and the concentric platinum ring. The potential of ring electrode was set to 0.4 V (vs. Hg/Hg_2Cl_2) to detect H_2O_2. The electron transfer number(n) and peroxide (H_2O_2) yield were calculated from the following equals:

$$H_2O_2(\%) = 200 \times \frac{\frac{I_r}{N}}{\frac{I_r}{N} + I_d}$$

$$n = \frac{4I_d}{I_d + \frac{I_r}{N}}$$

Where I_d is the disk current, I_r is the ring current, N = 0.249 is the collection efficiency constant of the ring.

AQY measurements:

The apparent quantum yield (AQY) was determined by exposing the system to illumination from a blue LED lamp with a wavelength of 420 nm and an intensity of 340 mW cm^{-2} (Kessil RoHS) for a duration of 1 hour. The AQY values reported in this study represent the maximum achievable results obtained after optimizing the quantities of photocatalysts, light intensities, and light absorption areas. Specifically, for the CPs at λ_0=420 nm, the average irradiation intensity of 30.8 mW cm^{-2} was measured using an ILT 950 spectroradiometer, while the irradiation area was precisely controlled at 3.2 cm^2. The AQY is calculated from equation (4).

$$AQY = \frac{N_e}{N_p} \times 100\%$$

$$N_p = \frac{IAt\lambda}{hc}$$

Here, N_e refers to the total number of electrons transferred in the reaction, and N_p stands for the number of incident photons. The symbol I indicates the light power density, which is measured in watts per square centimeter (W cm^{-2}). Symbol A represents the area of the incident light, measured in square centimeters (cm^2). Lambda (λ) signifies the wavelength of the incident light and it is measured in nanometers (nm), while t assigned for the time is calculated in seconds (s). h and c stand for the Planck's constant (6.62 x 10-34 J s^{-1}) and speed of light (3.0 x 108 m s^{-1}) respectively.

These parameters form critical components in the related equations and are typically used to study the interaction of light with specific materials under set conditions.

Calculation:

All DFT calculations were conducted utilizing the quickstep component of the CP2K software package. Within the structure of the Gaussian plane wave approach, CP2K employs Gaussian-type orbital functions for the depiction of the Kohn-Sham matrix. Additionally, an auxiliary plane wave basis is utilized for the portrayal of the electron density, with the density cutoff set at 500 Ry. The pseudopotentials by Goedecker, Teter, and Hutter (GTH), along with MOLOPT basis sets, were chosen. In every instance, the k-point sampling was confined to the Γ-point. The van der Waals correction through Grimme's DFT-D3 model was implemented as well.[3, 4] The DC-CP-Ph, CP-Ph, DC-CP-BP, and CP-BP structures were constructed for the computation of the H_2O_2 evolution reaction free energy. The single-point energies of all compounds were determined via the Gaussian function B3LYP/6-311G** in the CP2K software. The Multiwfn 3.8(dev) and VMD software were applied for the analysis of the computed results.

The ΔG of each elementary step was obtained by minus the Gibbs free energy of product with the Gibbs free energy of reactant. The Gibbs free energy of each model was calculated with eq.:

$$G = E + ZPE - TS \qquad (1)$$

where G, E, ZPE, and TS are the Gibbs free energy, energy, zero–point energy, and entropy, respectively.

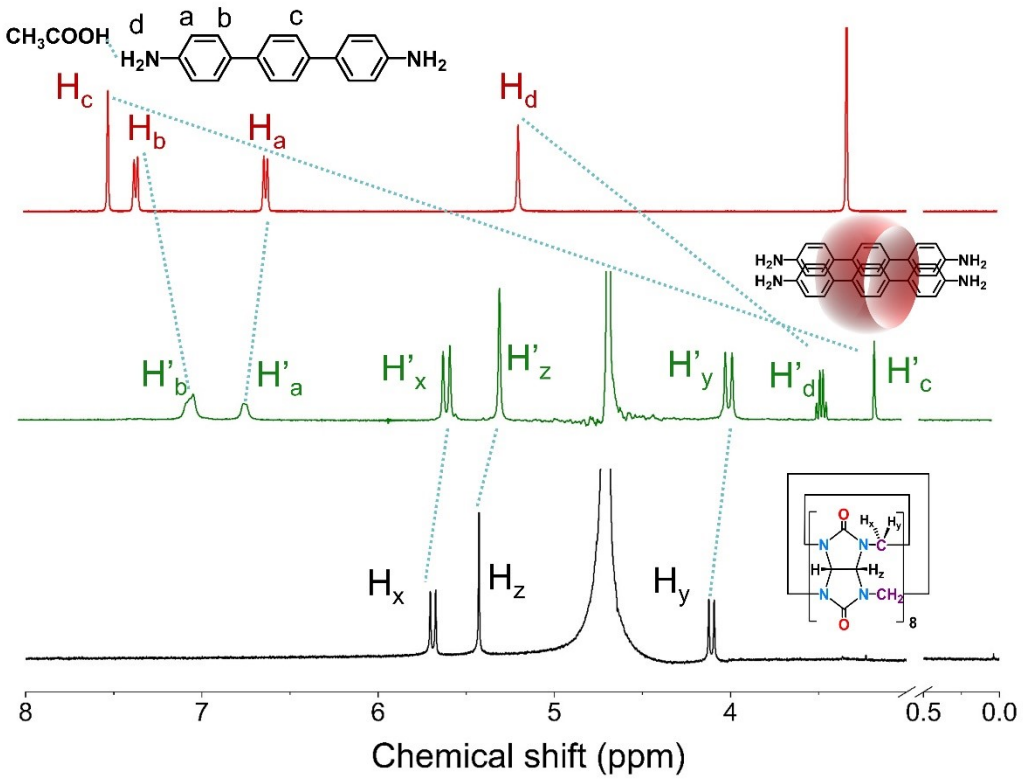

Figure S1 The ^{1}H NMR spectroscopy for DTP (red), d-DTP-CB8 (green) and CB[8] (black).

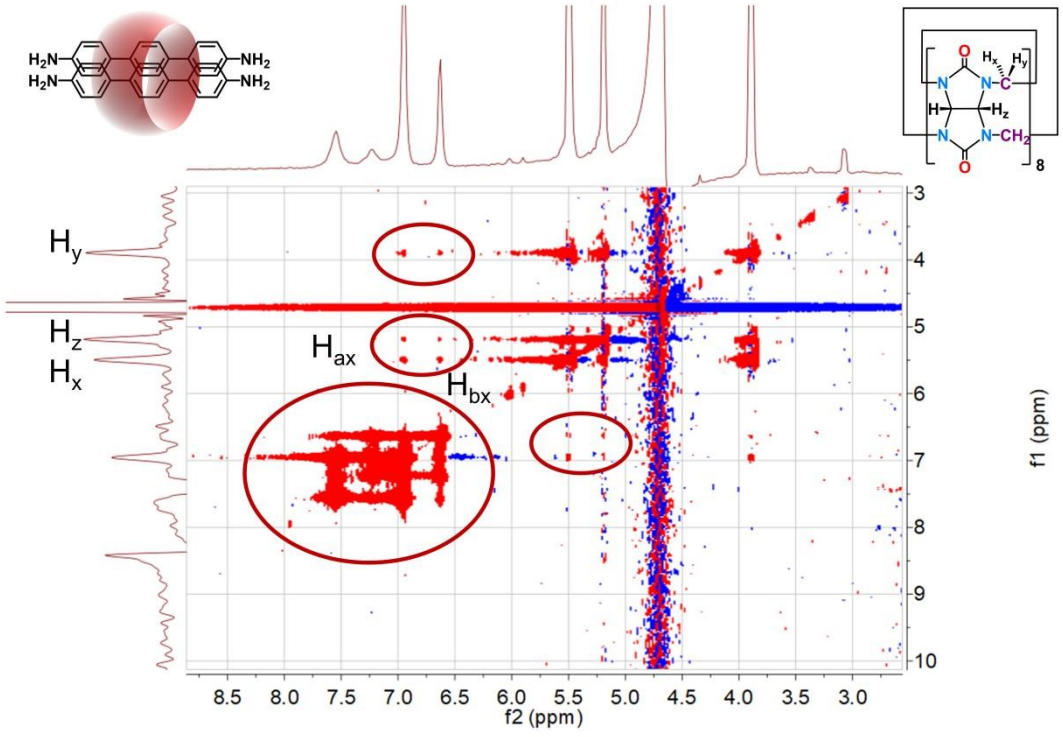

Figure S2 2D NOESY NMR spectrum of d-DTP-CB8.

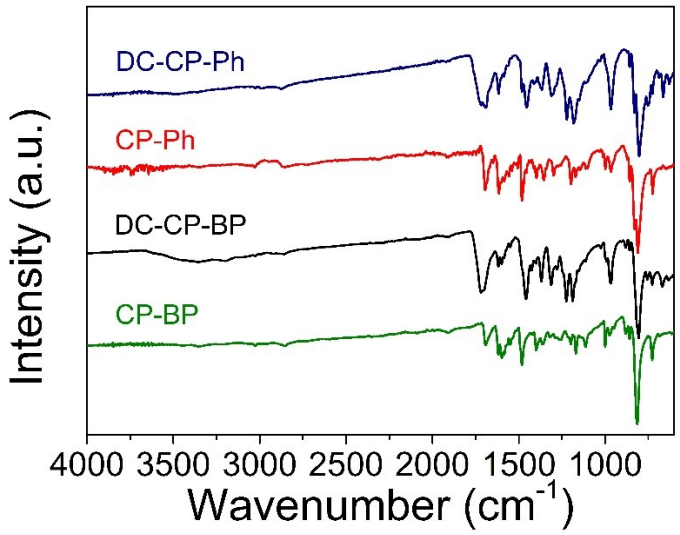

Figure S3 FTIR spectrum of CPs.

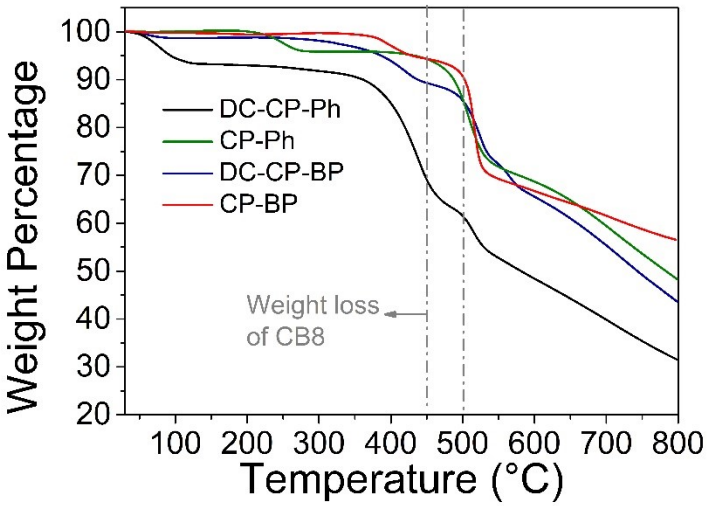

Figure S4 TGA of CPs at N_2 atmosphere.

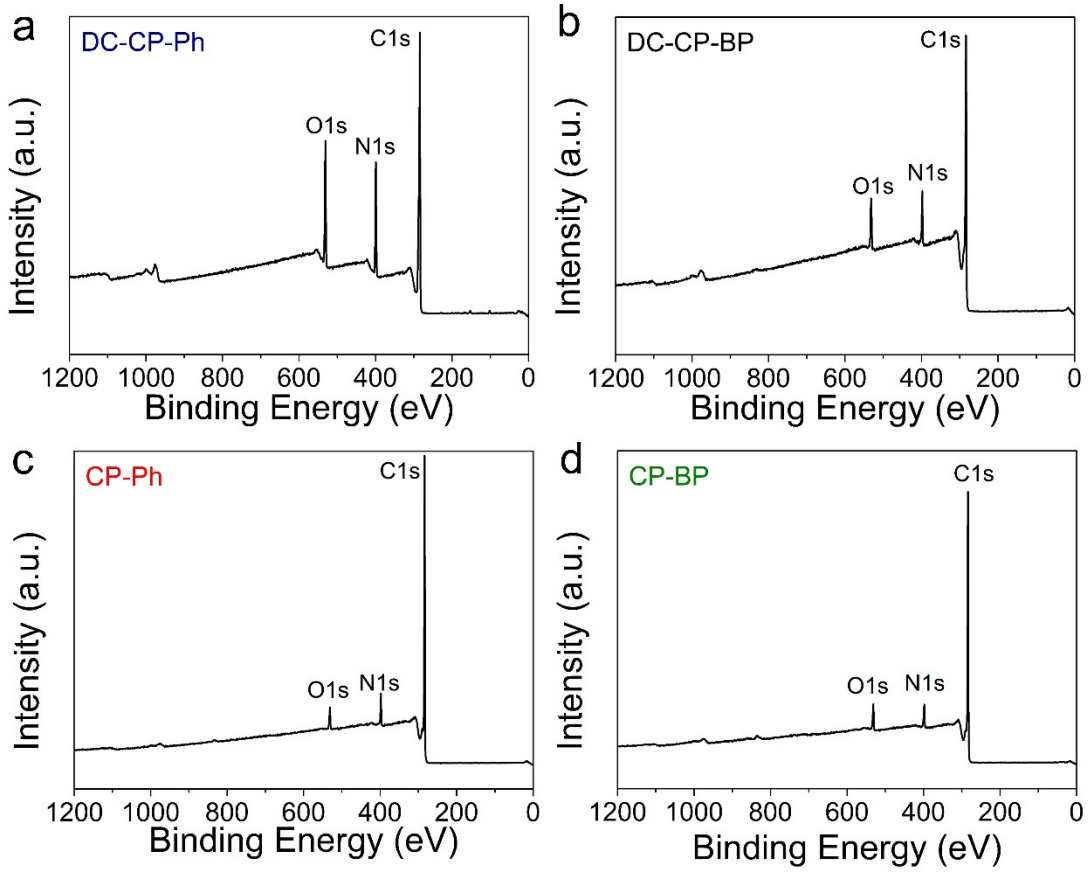

Figure S5 XPS survey spectrum of CPs.

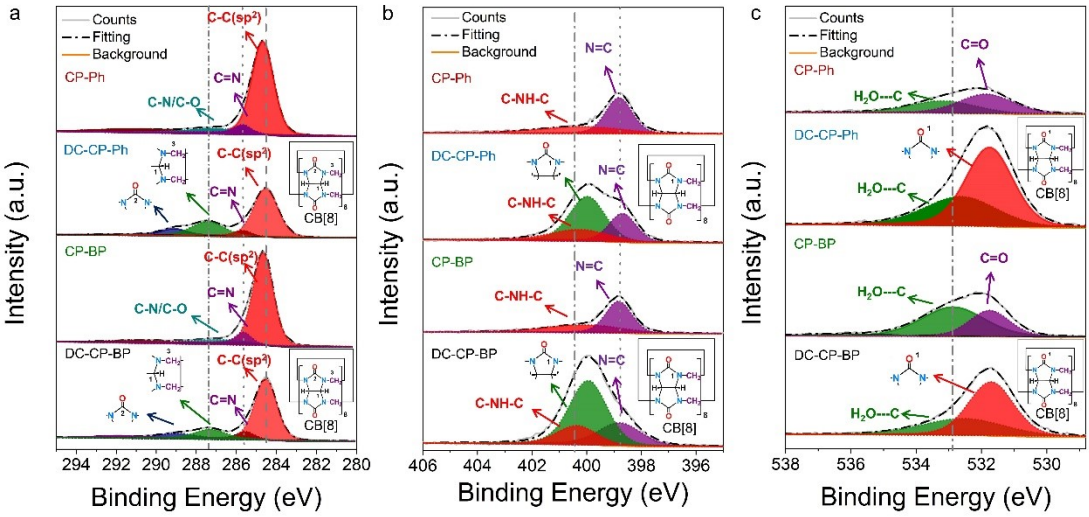

Figure S6 (a) High-resolution C 1s XPS spectra of CPs, (b) N 1s XPS spectra of CPs, (c) O 1s XPS spectra of CPs

Table S1. Peaks area and atomic ratios of C 1s configurations for CPs.

Samples	C−C(sp^2) (~284.6 eV) ratio	C=N (~285.5 eV) ratio	C(1) and C(3) of CB8 and C-N/C-O (~287.3 eV) Area/ratio	C(2) of CB8 (~289.1eV) Area/ratio	C content Ratio %
DC-CP-BP	128051 (284.58 eV)	10102/5.6%	27354/15.3%	13333/7.5%	80.7
CP-BP	191533 (284.78 eV)	11591/5.3%	14699/6.8%	-	89.0
DC-CP-Ph	111811 (284.63 eV)	7500/4.3%	42149/24.1%	13688/7.8%	78.1
CP-Ph	178976 (284.71 eV)	15198/7.3%	14104/6.8%	-	89.3

The peak at 284.56 eV shown in the table is attributed to the C-C (sp^2) peak of the benzene ring in the polymer chain, which has the highest proportion among the four materials, indicating that all four materials have a polymer structure with a benzene ring as the main chain. The peak at 285.5 eV is attributed to the imine bond in the polymer chain. Additionally, characteristic peaks of the cucurbituril ring were observed in both DC-CP-Ph and DC-CP-BP, where the C(1) and C(3) peaks of the cucurbituril ring overlapped with the C-N/C-O peaks of the main chain, further demonstrating the mass proportion of the cucurbituril molecule locked in the main chain structure.

Table S2. Peaks area and atomic ratios of N 1s configurations in COPs**.**

Samples	N=C (~398.7 eV) Area/ratio	N(1) of CB8 (400.0 eV) Area/ratio	C-NH-C (~400.3 eV) Area/ratio	N content Ratio %
DC-CP-BP	11816/26.4%	23356/52.2%	9577/21.4%	12.0
CP-BP	12352/59.1%	-	8551/40.9%	5.5
DC-CP-Ph	15012/24.3%	35846/58.0%	11008/17.8%	12.9
CP-Ph	14332/62.1%	-	8735/37.9%	6.2

Compared to SC-CPs, the nitrogen content in DC-CPs is significantly increased, with the additional portion attributable to the introduction of CB[8]. Moreover, the characteristic peak at 400.0 eV corresponds to the C-N bonds within CB[8]. Analysis of the distribution of bond proportions reveals the successful incorporation of cucurbit[8]uril into the polymer chains.

Table S3. Peaks area and atomic ratios of O 1s configurations in CPs.

Samples	C=O (~531.6 eV) Area/ratio	O(1) (~531.7 eV) Area/ratio	H_2O-----C (~533.2eV) Area/ratio	O content Ratio %
DC-CP-BP	-	27263/64.0%	15347/36.0%	7.3
CP-BP	11822/27.7 %	-	20443/48.0%	5.5
DC-CP-Ph	-	41824/64.3%	23221/35.7%	9.0
CP-Ph	16847/67.0 %	-	8282/33.0%	4.5

Table S4. Details regarding the specific surface area, pore size distribution and pore volume of CPs.

Samples	S_{NLDFT}[a] (m^2 g^{-1})	S_{BET} [b] (m^2 g^{-1})	Pore Diameter[c] (nm)	Fitting error (%)	V_{NLDFT} (cm^3 g^{-1})
DC-CP-BP	15.90	20.03	1.14	1.74	0.036
CP-BP	37.65	43.67	1.19	1.62	0.112
DC-CP-Ph	32.16	35.74	1.35	1.63	0.079
CP-Ph	44.20	51.78	1.48	1.45	0.100

[a] Surface area determined by the NLDFT method. [b] Surface area determined by the BET method. [c] Pore volume calculated at P/P_0=0.99.

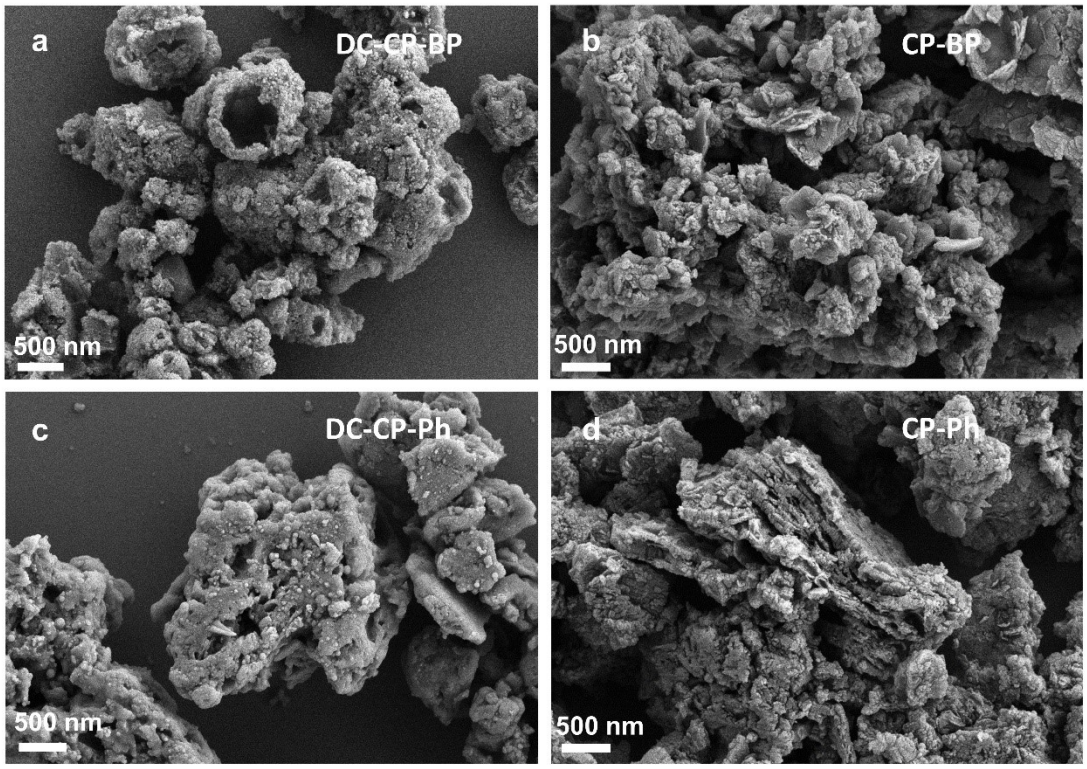

Figure S7 SEM images of corresponding CPs

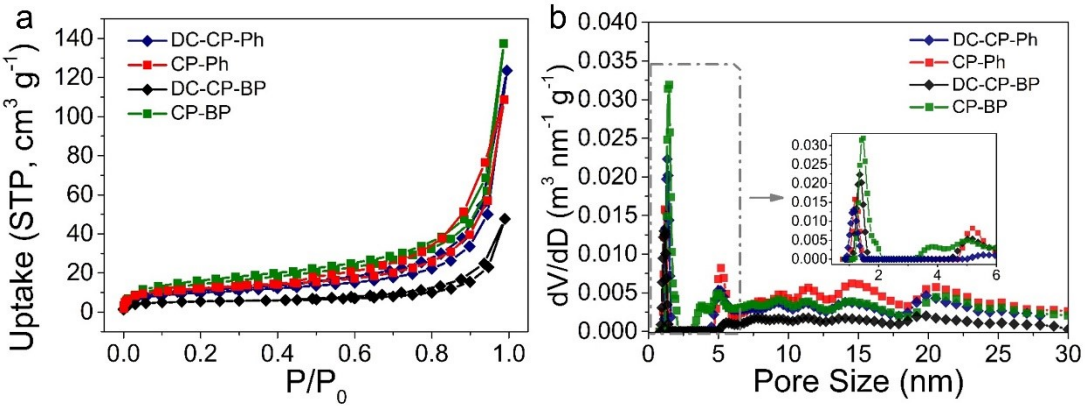

Figure S8 (a) N_2 adsorption/desorption isotherms and (b) corresponding pore size distributions of COPs.

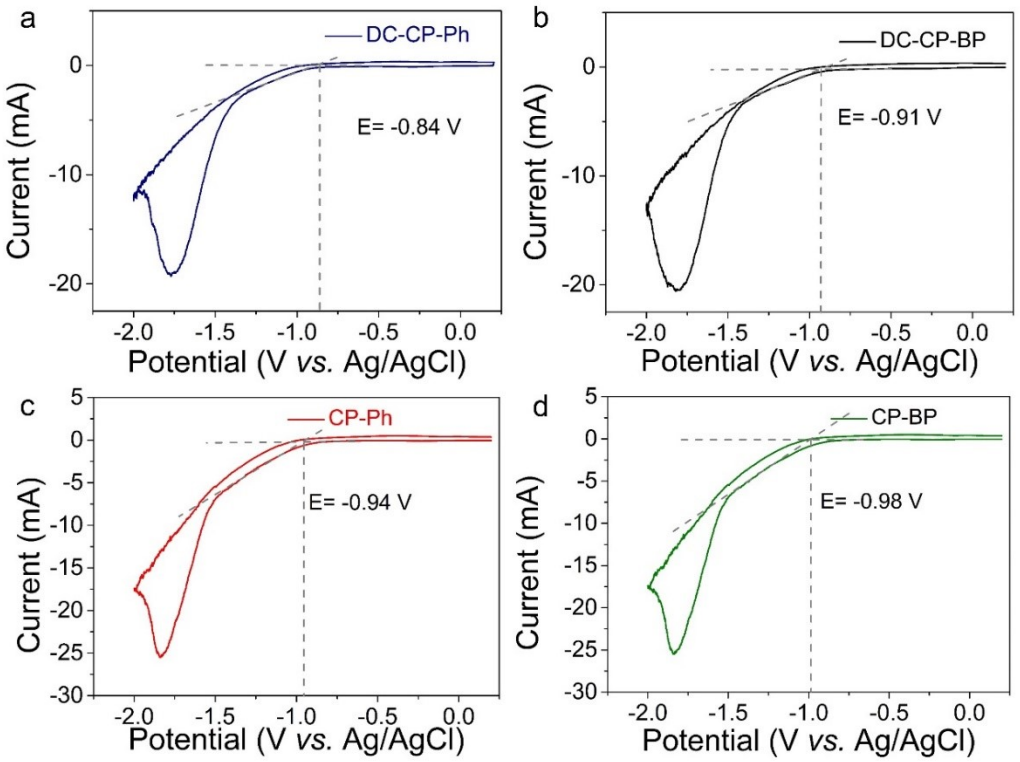

Figure S9 Cyclic voltammetry (CV) measurements in a three-electrode cell system with Ag/AgCl as reference electrode.

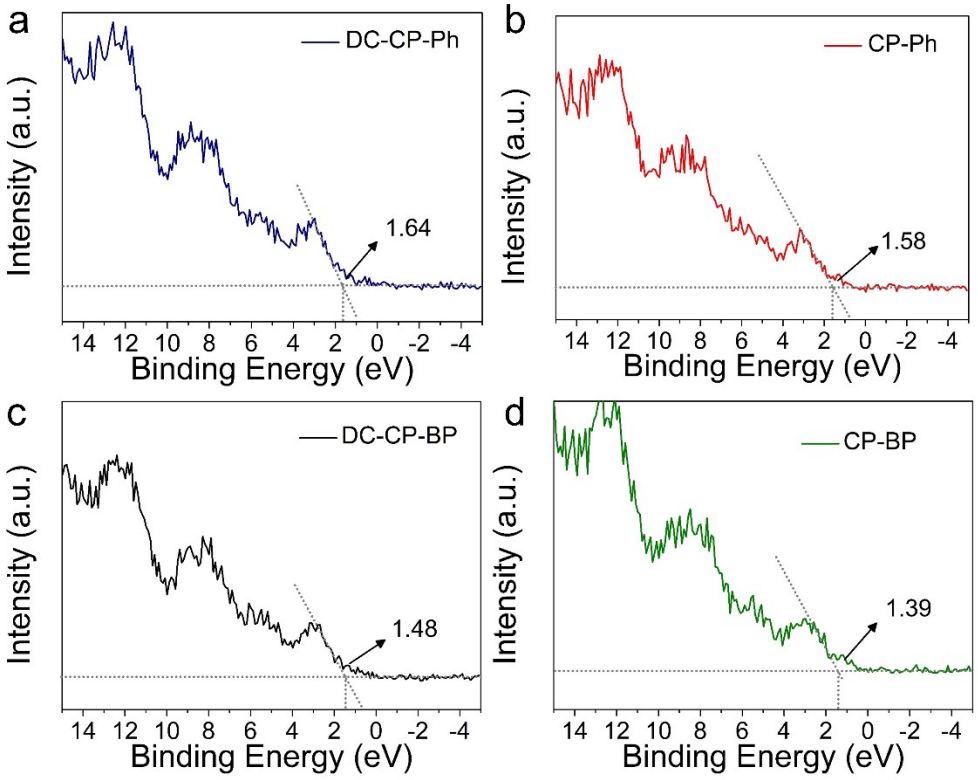

Figure S10 VB-XPS spectra of CPs.

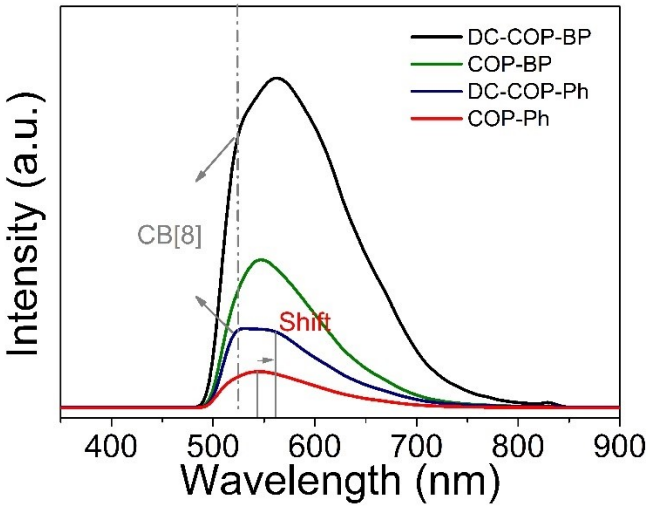

Figure S11 Steady-state fluorescence spectroscopy of CPs.

The fluorescence spectrum of DC-CPs exhibits a certain red shift relative to that of SC-CPs. These were attributed to the interaction between two polymer chain. The dual-chain structure leads to a reduction in rotational freedom over the single-chain structure, which may increase the energy gap between electronic transition levels in the whole conjugated system and thus result in a red shift of the fluorescence emission spectrum.

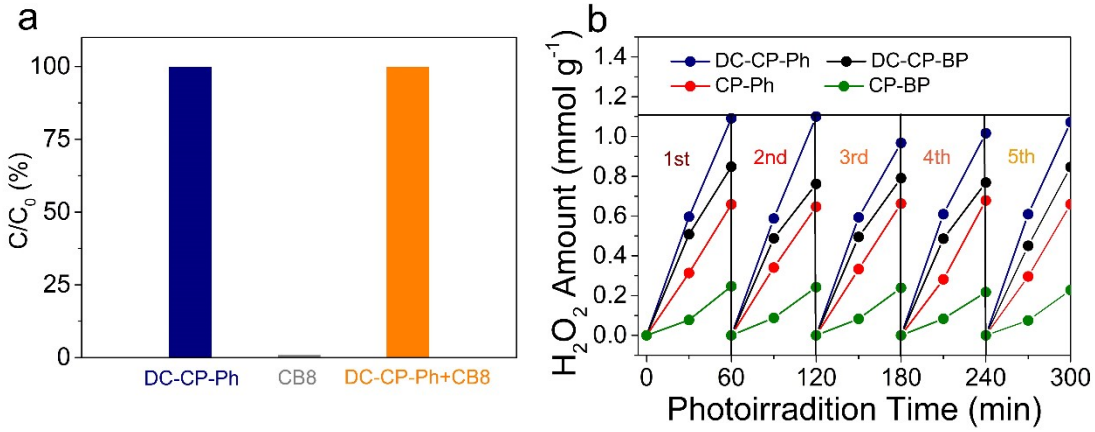

Figure S12 (a) Hydrogen peroxide production using DC-CP-Ph (blue), pure CB8 (gray) and mixture of DC-CP-Ph and CB8 (1:0.5) (orange) as catalyst. The concentration of H_2O_2 production for DC-CP-Ph was set as C_0. (b) The cyclic tests for the photocatalytic hydrogen peroxide production of CPs involved removing and drying the catalyst after each 1-hour test. This process was repeated for a total of five cycles.

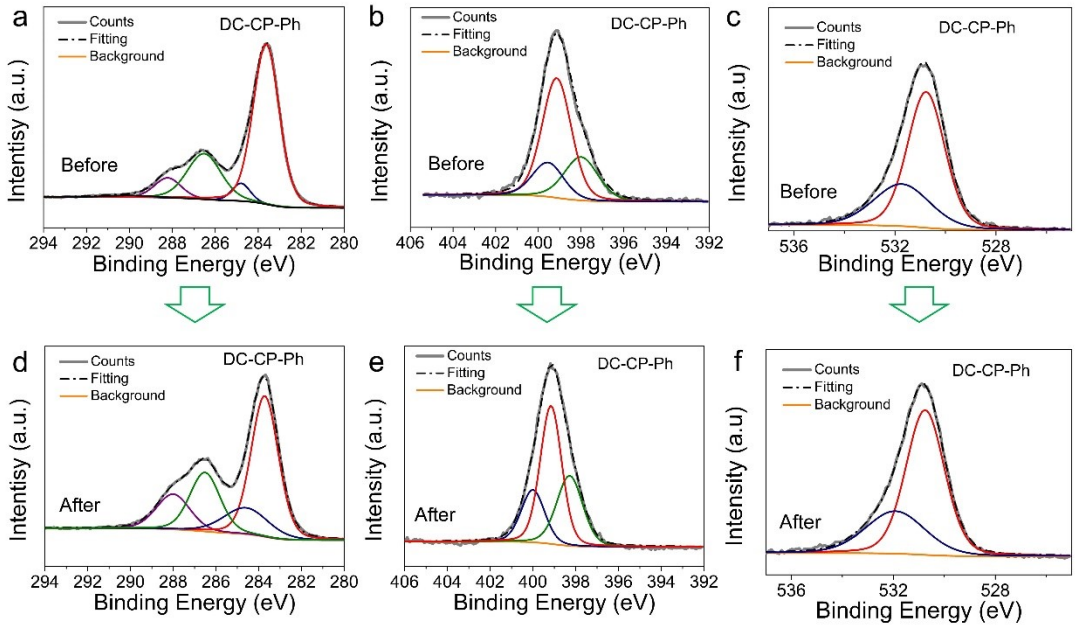

Figure S13 High-resolution C 1s, N 1s and O 1s XPS spectra of DC-CP-Ph obtained after three cycles of photocatalytic tests along with that before photocatalysis.

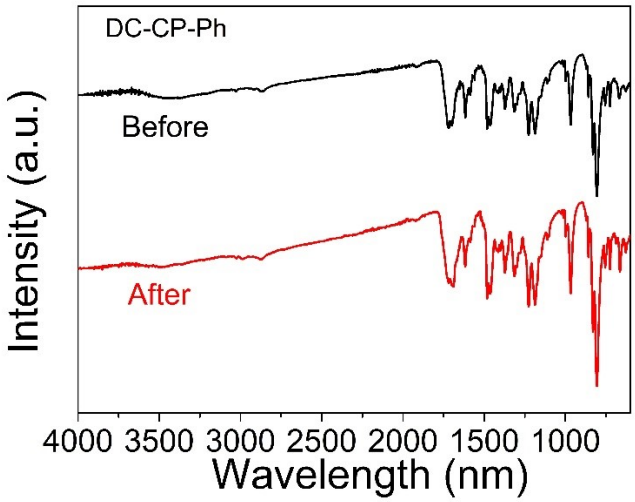

Figure S14 FTIR spectrum of DC-CP-Ph obtained after three cycles of photocatalytic tests along with that before photocatalysis.

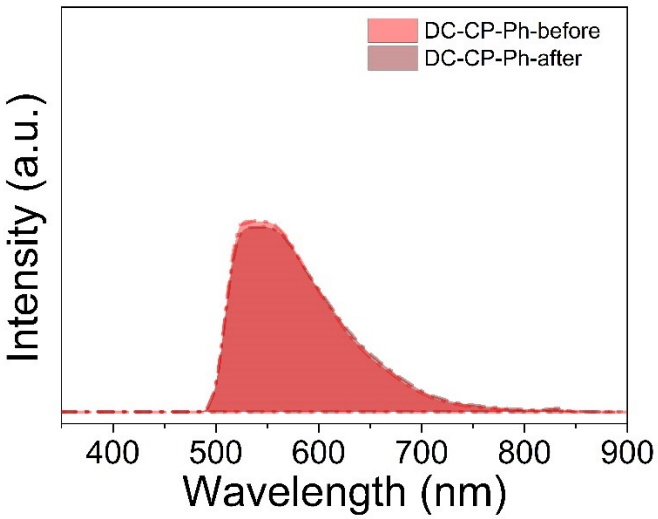

Figure S15 PL spectrum of DC-CP-Ph obtained after three cycles of photocatalytic tests along with that before photocatalysis.

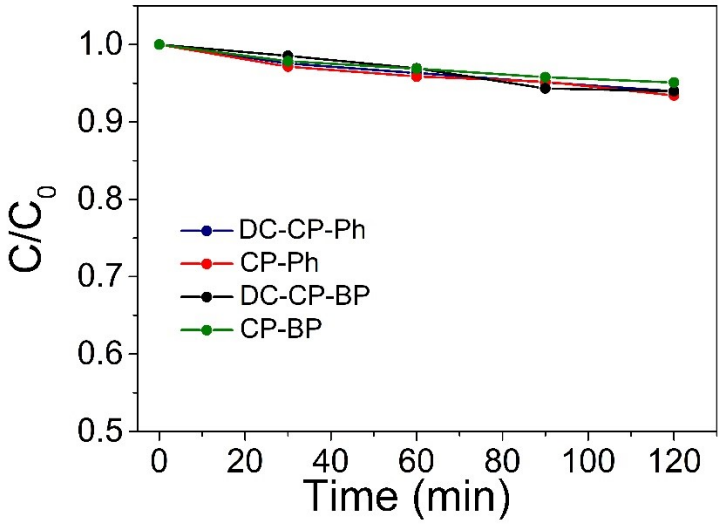

Figure S16 Photocatalytic decomposition of H_2O_2 (C_0=200 μL 30% H_2O_2 in 10 mL water) in pure water under visible light irradiation over different CPs.

Table S5. Comparison of commonly reported photocatalysts for H_2O_2 generation in pure water/in the presence of sacrificial agents with other photocatalysts from recent years.

Samples	H_2O_2 evolution rate (μ mol g^{-1} h^{-1})	Reaction Conditions	Reference
DC-CP-Ph, DC-CP-BP	1090, 848	0.5 mg-Cat. mL^{-1}, LED (340 mW cm^{-2}, λ>420 nm), O_2- equilibrated, pure water, 20 ℃	This Work
TZ-COF	268	1.5 mg-Cat. mL^{-1}, 300 W Xe lamp (λ>420 nm), O_2 atmosphere, pure water, 25 ℃	5
TTF-PDI-COF	480	0.25 mg-Cat. mL^{-1}, LED, λ=420 nm, O_2-equilibrated, pure water, 25 ℃	6
PCNHS-17	174	0.5 mg-Cat. mL^{-1}, Xe lamp (100 mW cm^{-2}, λ>420 nm), O_2-equilibrated, pure water, 25 ℃	7
N_0-COF	1570	0.5 mg-Cat. mL^{-1}, LED, λ=495 nm, O_2-equilibrated, pure water, 30 ℃	8
HMP-PPR	103	0.5 mg-Cat. mL^{-1}, 340 Xe lamp (λ>420 nm), 1 atm O_2, water/IPA (8:2 v/v)	9
CNP-s	3200	0.1 mg-Cat. mL^{-1}, 1440 W Xenon (λ>420 nm), O_2-equilibrated, 0.1 M H_2SO_4 solution	10
COF-TfpBpy	649.7	0.5 mg-Cat. mL^{-1}, Xe lamp (λ>420 nm), O_2-equilibrated, pure water, 25 ℃	11
Pd/A/$BiVO_4$	805.9	1 mg-Cat. mL^{-1}, 300 W Xe lamp (λ>420 nm), O_2-equilibrated, 0.1 M phosphate buffer (pH 3.0), 0 ℃	12
P,N−C@CNHS	239.5	0.5 mg-Cat. mL^{-1}, Xe lamp (100 mW cm^{-2}, λ>420 nm), O_2, isopropanol in water (10%), 25 ℃	13
Py-Da-COF	461	1 mg-Cat. mL^{-1}, 300 W Xe light (λ>420 nm), O_2, pure water, room temperature	14
TAPT-TFPA COFs@PdICs	2143	0.5 mg- Cat. mL^{-1}, 300 W Xe lamp (1.5 G, λ>420 nm), O_2, 10% ethanol solution, room temperature	15
rGO@MRF-0.5	861	0.25 mg- Cat. mL^{-1}, 300 W Xe lamp (λ>420 nm), continuous O_2, pure water, 25 ℃	16
Co_{14}-(L-CH_3)$_{24}$	146.6	0.5 mg- Cat. mL^{-1}, 300 W Xe lamp (300<λ<1100 nm), O_2-equilibrated, pure water, 25 ℃	17

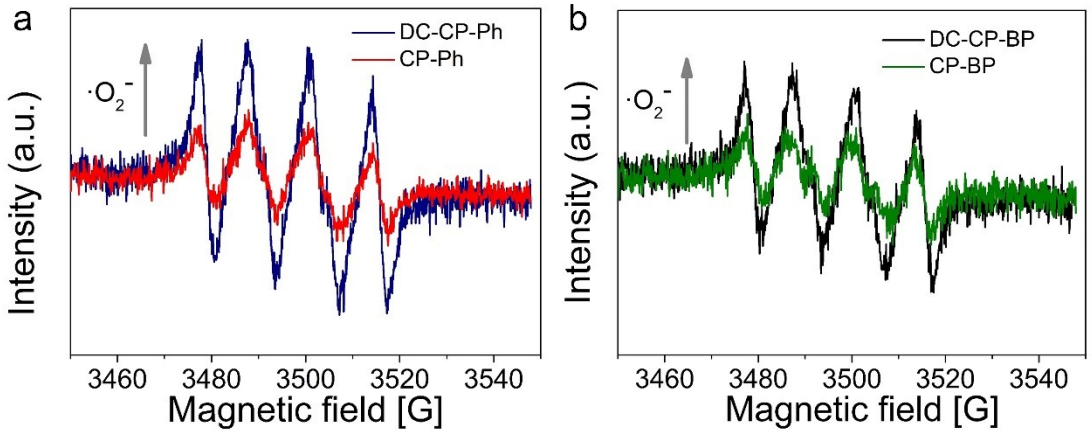

Figure S17 Detecting of $O_2^{\bullet-}$ in EPR trapping experiments of CPs, (a) DC-CP-Ph and CP-Ph and (b) DC-CP-BP and CP-BP.

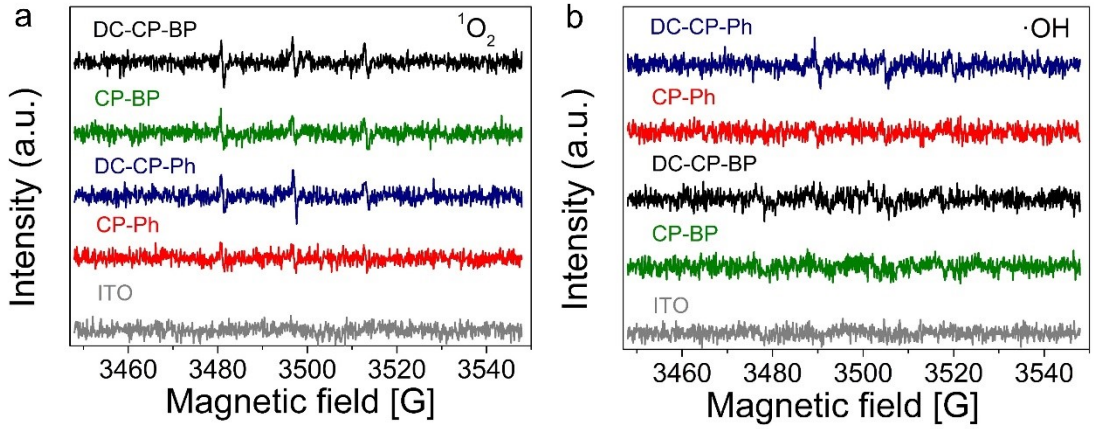

Figure S18 Detecting of $^1O_2$ and •OH in EPR trapping experiments of CPs, (a) DC-CP-Ph and CP-Ph and (b) DC-CP-BP and CP-BP.

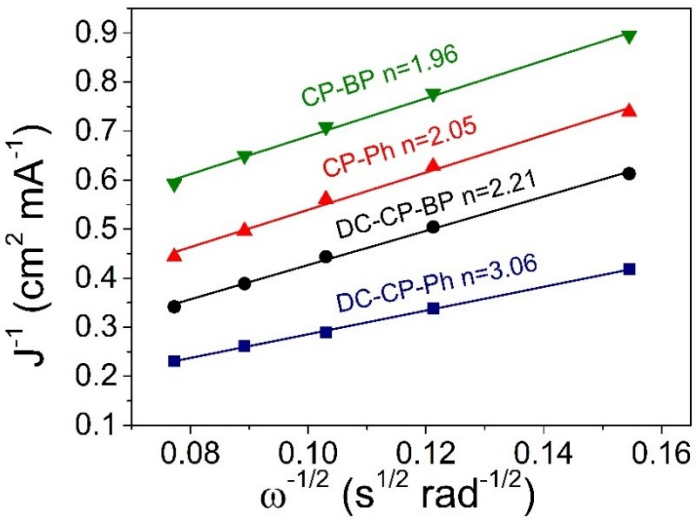

Figure S19 The Koutecky-Levich plots obtained by RDE measurements.

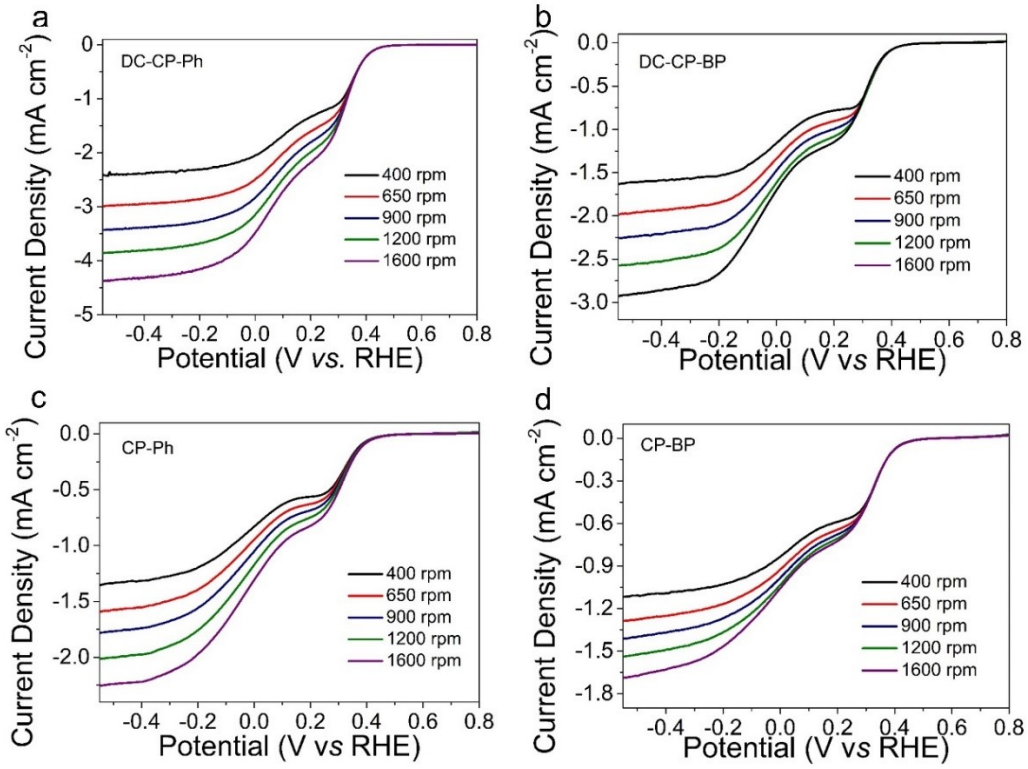

Figure S20 Linear-sweep Rotating disk electrode (RDE) voltammograms over different CPs.

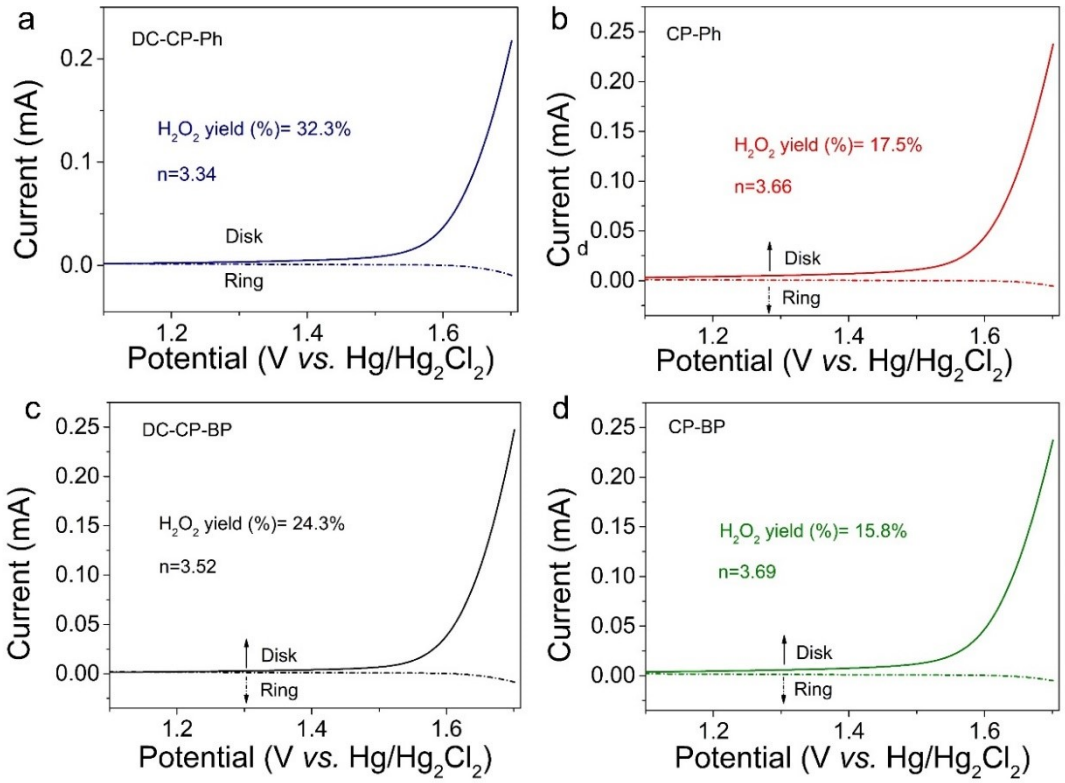

Figure S21 Rotating ring-disk electrode voltammograms obtained in 1M KCl as electrolyte. 0.6 V versus Ag/AgCl was set to detect H_2O_2.

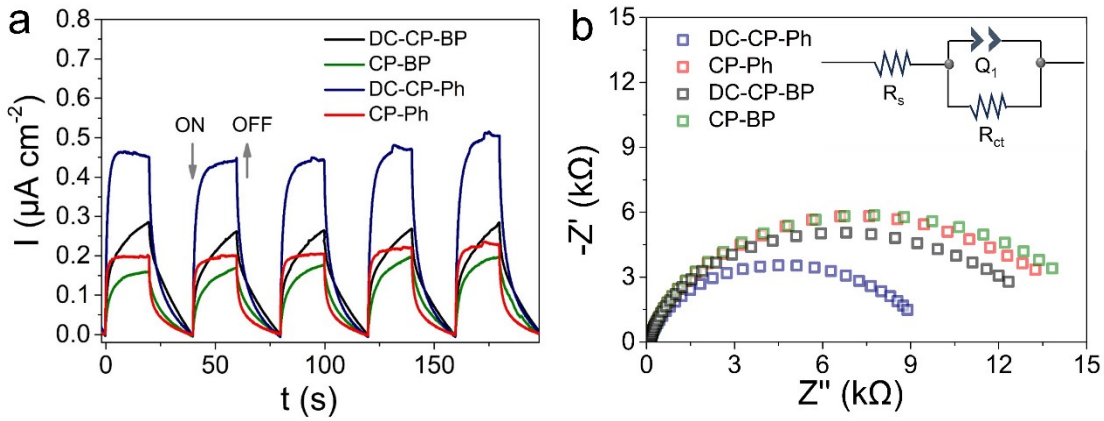

Figure S22 Photoelectrochemical test of CPs. (a) Photocurrent analysis. (b) EIS test, where insertion plot the equivalent circuit fitting.

Table S6. The fitting results of electrochemical impedance spectroscopy (EIS) for CPs based on the equivalent circuit model.

Samples	R_s[a] (Ω)	R_{ct}[b] (kΩ)	CPE-T[c] ($\times 10^{-4}$)
DC-CP-BP	102.5	12.06	0.03
CP-BP	106	13.12	0.031
DC-CP-Ph	119.7	8.16	0.032
CP-Ph	126.5	12.60	0.029

In this model, [a]R_s denotes the interfacial contact resistance, [b]R_{ct} signifies the charge transfer resistance, and [c]CPE-T refers to the time scale component of the Constant Phase Element.

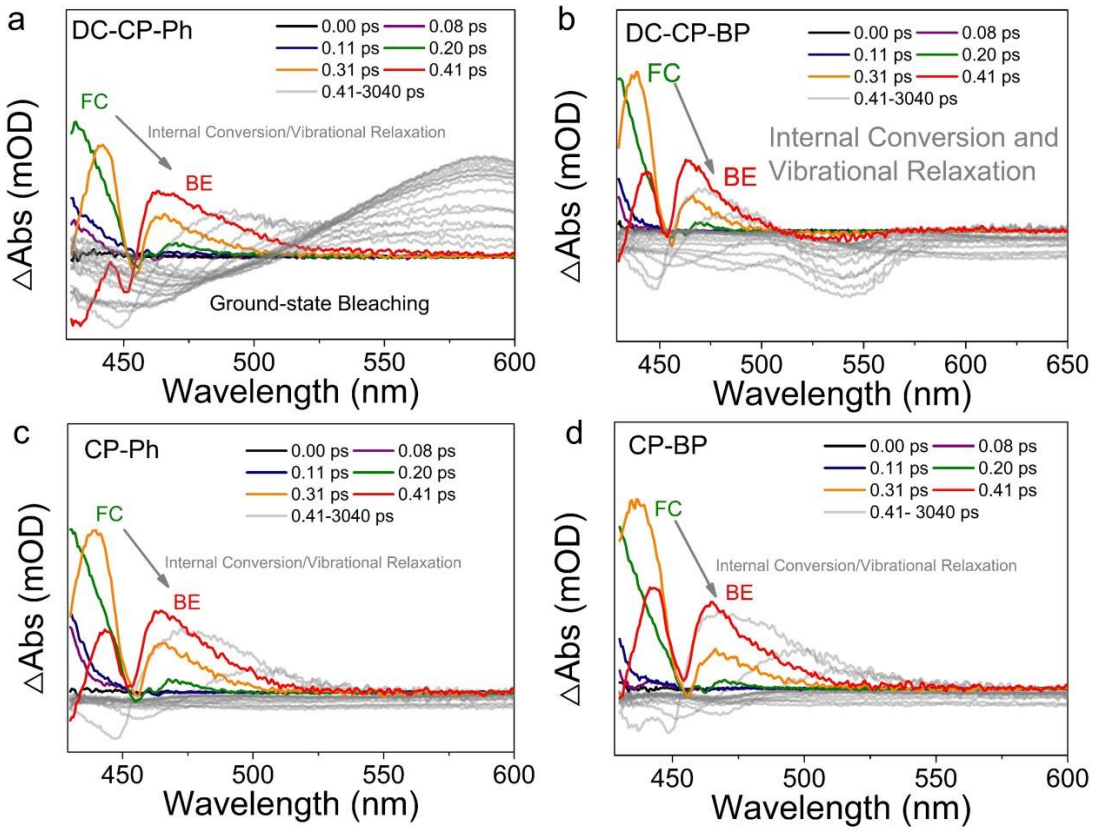

Figure S23 Femtosecond (fs) time-resolved transient absorption (TA) spectra (pump at 420 nm) of (a) DC-CP-Ph, (b) DC-CP-BP, (c) CP-Ph and (d) CP-BP in DMF at different delay times from 0.00 to 0.41 ps. All CPs are observed to undergo a transition from the Franck-Condon (FC) state to the bound exciton (BE) state on a picosecond timescale. This reveals the process by which the material absorbs photon energy and subsequently transfers that energy.

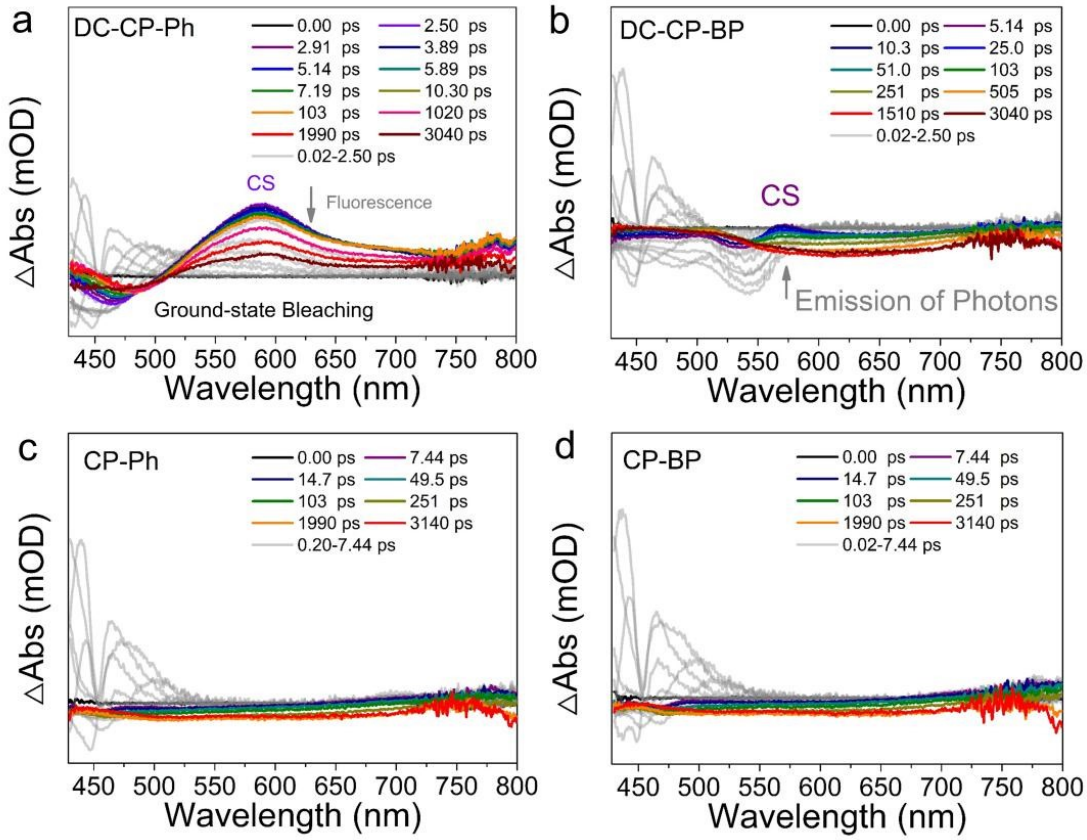

Figure S24 Femtosecond (fs) time-resolved transient absorption (TA) spectra (pump at 420 nm) of (a) DC-CP-Ph, (b) DC-CP-BP, (c) CP-Ph and (d) CP-BP in DMF at different delay times from 7.44 to 3140 ps. DC-CPs are observed to undergo a transition from the Franck-Condon (FC) state to charge transfer (CT) processes on a nanosecond timescale. Charge transfer (CT) processes can persist on the nanosecond timescale. However, such processes were not observed in SC-CPs. This observation elucidates the pathways of energy transfer and dissipation.

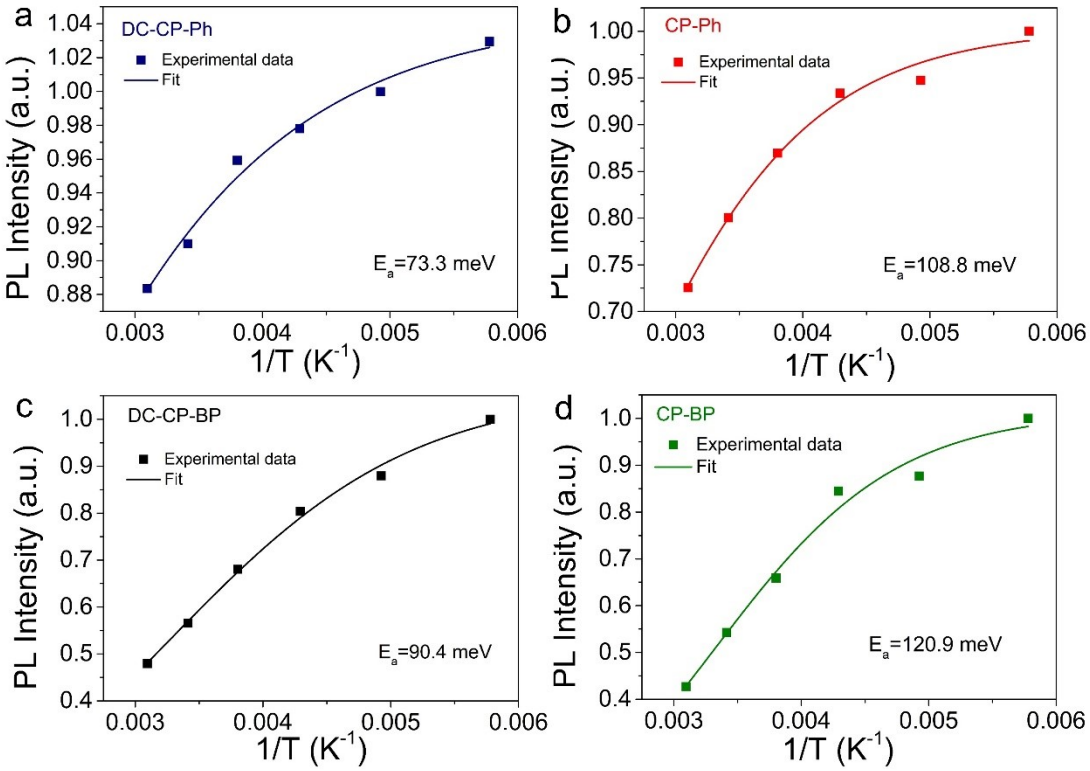

Figure S25 Integrated PL intensities of (a) DC-CP-Ph, (b) DC-CP-BP, (c) CP-Ph and d) CP-BP obtained from temperature-dependent measurements.

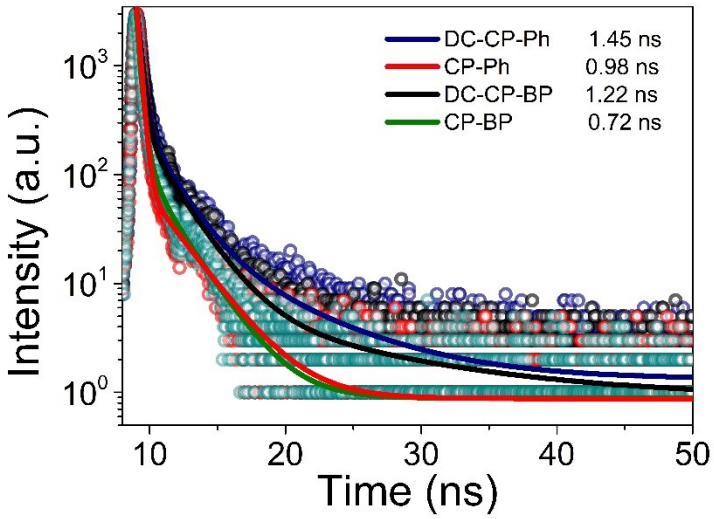

Figure S26 The TPRL spectrum for CPs.

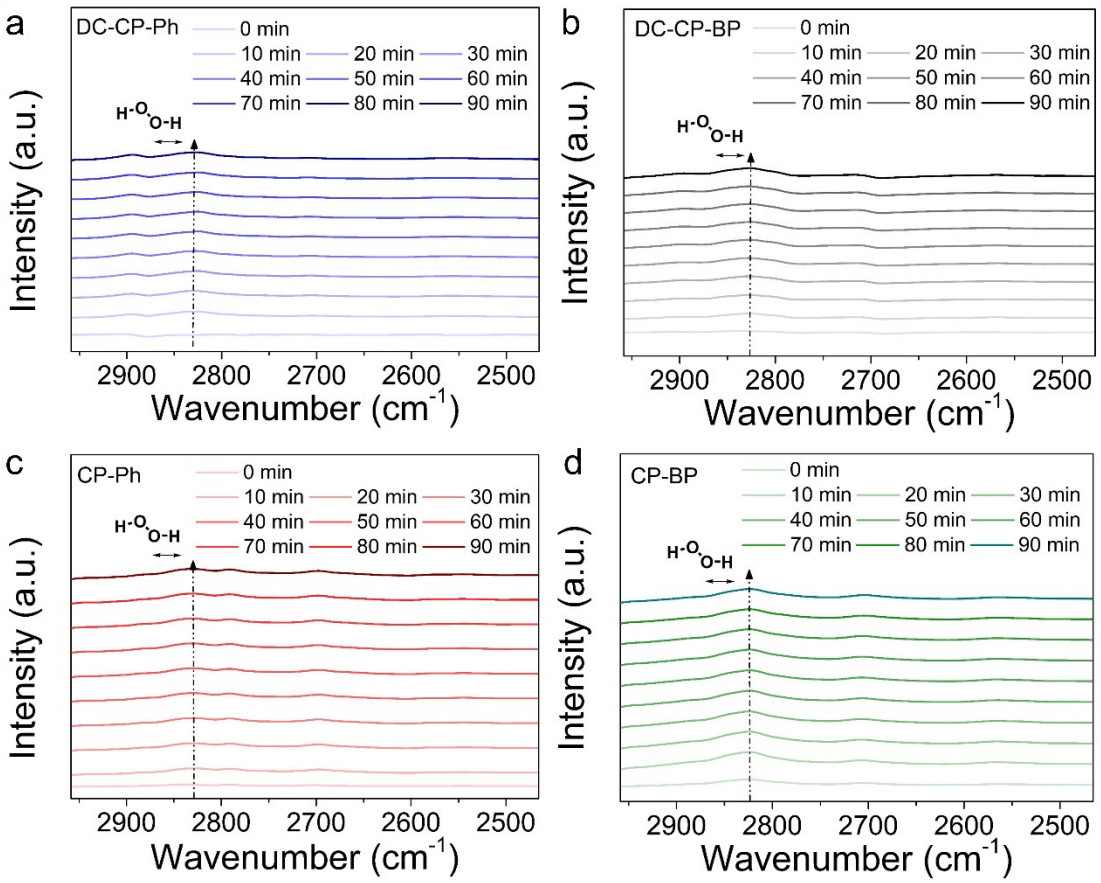

Figure S27 (a)–(d) In situ DRIFT spectra of CPs recorded during photocatalytic H_2O_2 evolution.

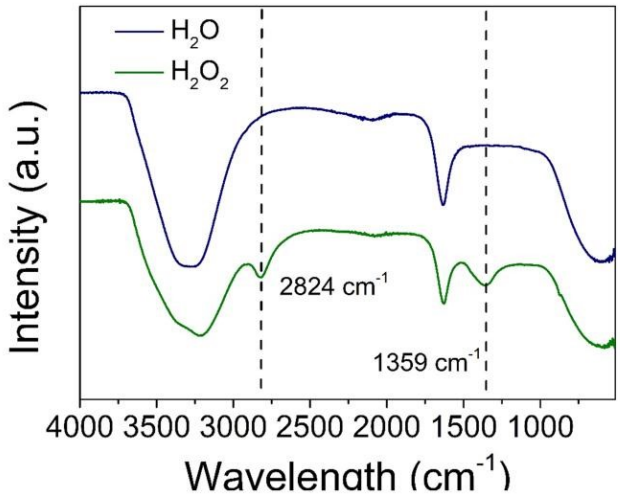

Figure S28 FTIR spectrum of H_2O and H_2O_2 with the same instrument with the in-situ DRIFT spectra.

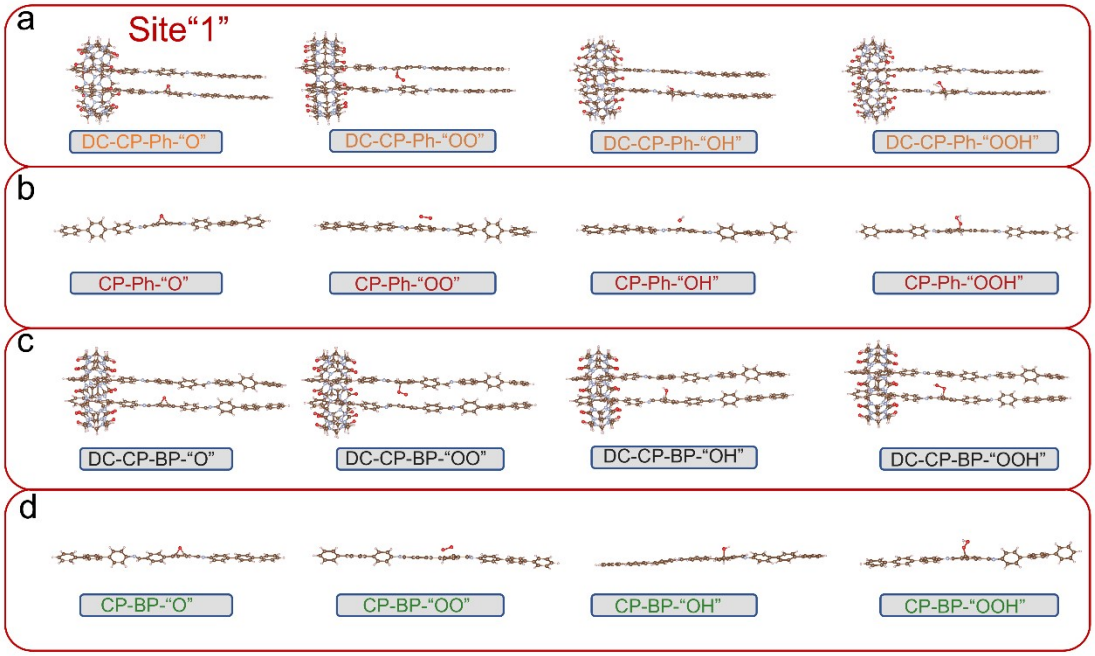

Figure S29 The depiction illustrates the calculated active sites for Gibbs free energies (in the units of eV), associated with O_2 adsorption on CPs at different, locations.

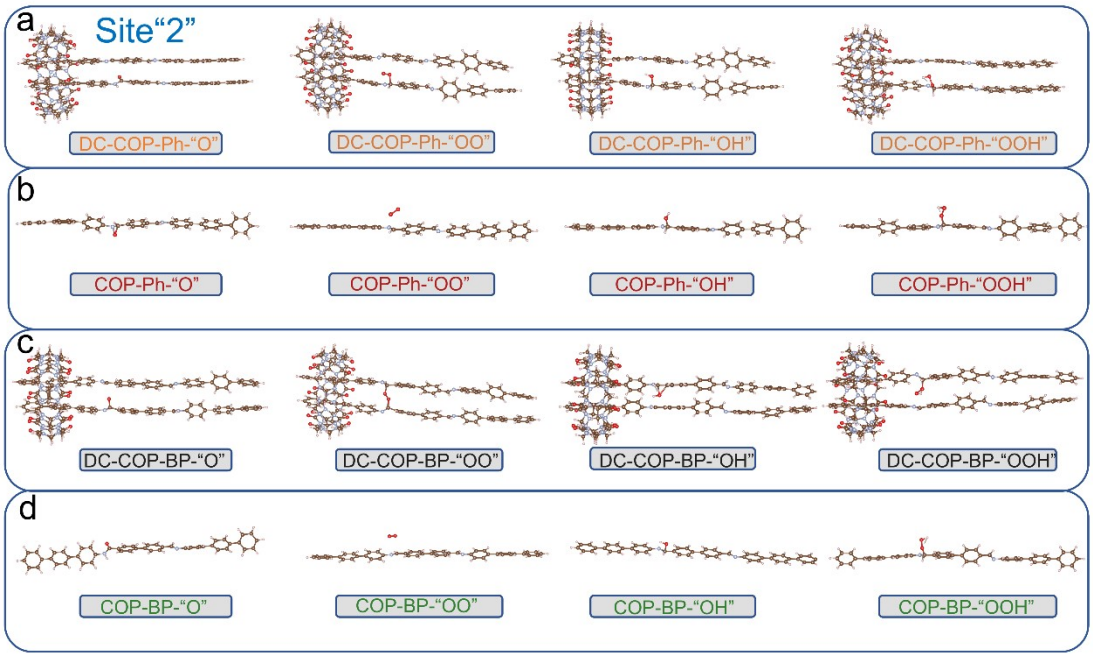

Figure S30 The depiction illustrates the calculated active sites for Gibbs free energies (in the units of eV), associated with O_2 adsorption on CPs at different "site 2" locations.

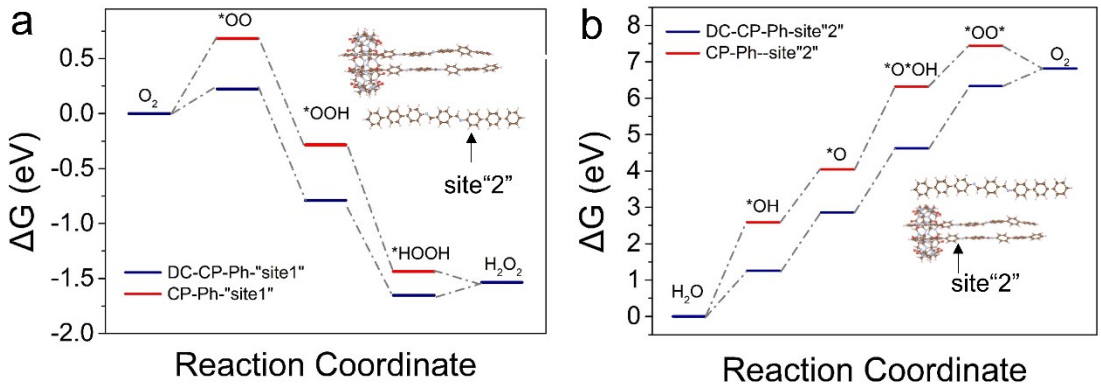

Figure S31 Calculated free energy diagrams of different pathways toward H_2O_2 production on active site“2” in DC-CP-Ph and CP-Ph. (a) oxygen reduction pathway and (b) water oxidation pathways.

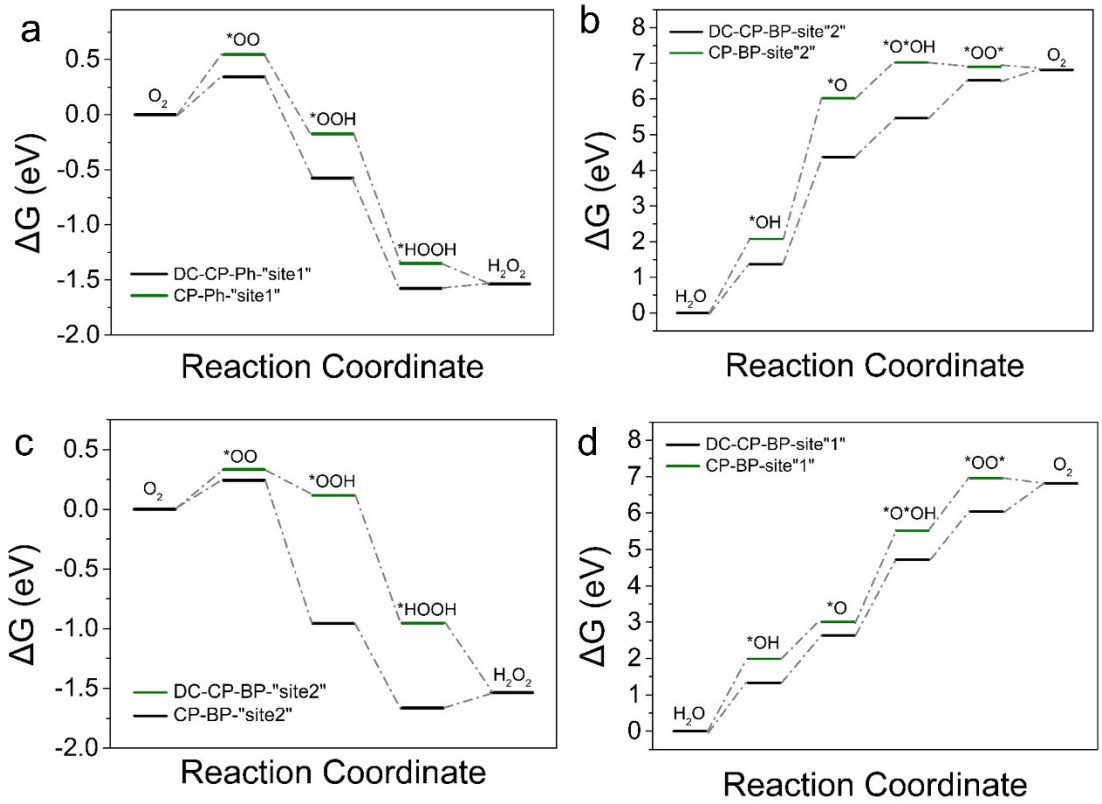

Figure S32 Calculated free energy diagrams of different pathways toward H_2O_2 production on active site“1” and site“2” in DC-CP-BP and CP-BP. (a) oxygen reduction pathway and (b) water oxidation pathways in site“1”, (c) oxygen reduction pathway and d) water oxidation pathways in site“2”

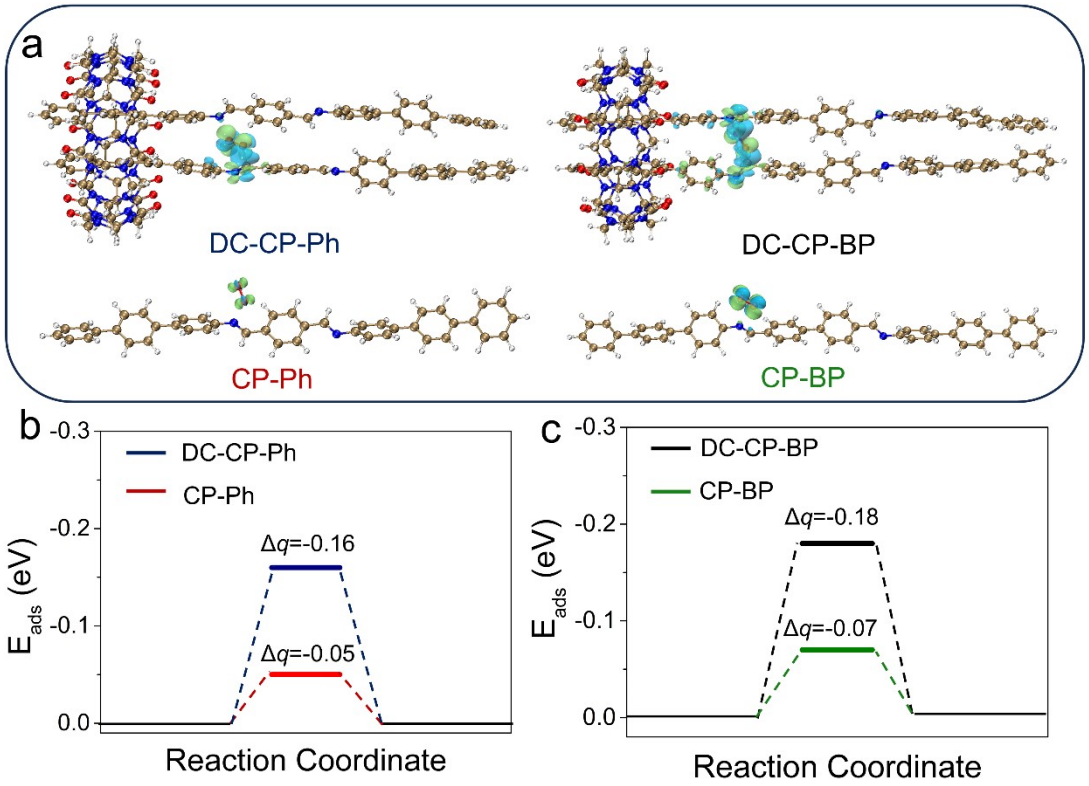

Figure S33 The Bader charges calculation of oxygen molecule for CPs on different central sites.

Reference

1. J. Kim, I.-S. Jung, S.-Y. Kim, E. Lee, J.-K. Kang, S. Sakamoto, K. Yamaguchi and K. Kim, *Journal of the American Chemical Society*, 2000, **122**, 540-541.
2. C. Li, W. Liu, X. Peng, L. Shao and S. Feng, *Chinese Journal of Aeronautics*, 2019, **32**, 1184-1189.
3. S. Grimme, J. Antony, S. Ehrlich and H. Krieg, *The Journal of Chemical Physics*, 2010, **132**.
4. H. J. Monkhorst and J. D. Pack, *Physical Review B*, 1976, **13**, 5188-5192.
5. Y. Mou, X. Wu, C. Qin, J. Chen, Y. Zhao, L. Jiang, C. Zhang, X. Yuan, E. Huixiang Ang and H. Wang, *Angewandte Chemie International Edition*, 2023, **62**, e202309480.
6. H. Xu, S. Xia, C. Li, Y. Li, W. Xing, Y. Jiang and X. Chen, *Angewandte Chemie International Edition*, 2024, **63**, e202405476.
7. X. Dang, R. Yang, Z. Wang, S. Wu and H. Zhao, *Journal of Materials Chemistry A*, 2020, **8**, 22720-22727.
8. S. Chai, X. Chen, X. Zhang, Y. Fang, R. S. Sprick and X. Chen, *Environmental Science: Nano*, 2022, **9**, 2464-2469.
9. S. Kumar, V. R. Battula, N. Sharma, S. Samanta, B. Rawat and K. Kailasam, *Journal of Materials Chemistry A*, 2022, **10**, 14568-14575.

10. H. Yang, C. Li, T. Liu, T. Fellowes, S. Y. Chong, L. Catalano, M. Bahri, W. Zhang, Y. Xu, L. Liu, W. Zhao, A. M. Gardner, R. Clowes, N. D. Browning, X. Li, A. J. Cowan and A. I. Cooper, *Nature Nanotechnology*, 2023, **18**, 307-315.
11. M. Kou, Y. Wang, Y. Xu, L. Ye, Y. Huang, B. Jia, H. Li, J. Ren, Y. Deng, J. Chen, Y. Zhou, K. Lei, L. Wang, W. Liu, H. Huang and T. Ma, *Angewandte Chemie International Edition*, 2022, **61**, e202200413.
12. M. Sun, X. Wang, Y. Li, H. Pan, M. Murugananthan, Y. Han, J. Wu, M. Zhang, Y. Zhang and Z. Kang, *ACS Catalysis*, 2022, **12**, 2138-2149.
13. X. Dang, X. Cui, H. Zhang, X. Chen and H. Zhao, *ACS Sustainable Chemistry & Engineering*, 2023, **11**, 13096-13107.
14. J. Sun, H. Sekhar Jena, C. Krishnaraj, K. Singh Rawat, S. Abednatanzi, J. Chakraborty, A. Laemont, W. Liu, H. Chen, Y.-Y. Liu, K. Leus, H. Vrielinck, V. Van Speybroeck and P. Van Der Voort, *Angewandte Chemie International Edition*, 2023, **62**, e202216719.
15. Y. Liu, L. Li, H. Tan, N. Ye, Y. Gu, S. Zhao, S. Zhang, M. Luo and S. Guo, *Journal of the American Chemical Society*, 2023, **145**, 19877-19884.
16. Q. Tian, X.-K. Zeng, C. Zhao, L.-Y. Jing, X.-W. Zhang and J. Liu, *Advanced Functional Materials*, 2023, **33**, 2213173.
17. J.-N. Lu, J.-J. Liu, L.-Z. Dong, J.-M. Lin, F. Yu, J. Liu and Y.-Q. Lan, *Angewandte Chemie International Edition*, 2023, **62**, e202308505.